Spacecraft orbit determination through a joint processing of imaging and radio-tracking data

Simone Andolfo[(1)], Antonio Genova[(1)], Pierluigi Federici[(1)], and Riccardo Teodori[(1)]

[(1)]*Sapienza - University of Rome, Department of Mechanical and Aerospace Engineering, Rome, Italy*
Email: {simone.andolfo, antonio.genova, pierluigi.federici, riccardo.teodori}@uniroma1.it

Abstract – **Autonomous navigation is a key requirement to expand the scientific return of the future space exploration missions. Novel guidance, navigation, and control systems are currently under development to support a precise reconstruction of the spacecraft trajectory through a combined processing of multi-sensor datasets. A joint analysis of ground-based radio-tracking data and image-based measurements, for example, can improve the estimation of the spacecraft trajectory by providing additional constraints based on the detection and tracking of relevant surface features (*e.g.*, craters). Numerical simulations based on a lunar orbiter are presented in this work to investigate the attainable accuracies of the proposed data-fusion orbit determination approach.**

I. INTRODUCTION

A precise reconstruction of the spacecraft trajectory is a key requirement to accomplish the challenging mission scientific tasks, and advanced data-fusion techniques are currently under development to enhance the orbit determination (OD) operations of the next-generation robotic probes. A combined processing of different data types, including radiometric [1], altimetric, and imaging data [2], can indeed enable an improved estimation of the spacecraft trajectory compared to solutions based on radio tracking data only.

Imaging data provide crucial information to better constrain the spacecraft position in the along- and across-track directions through the detection and tracking of features displaced across the surface of the target body (*e.g.*, craters). Since imaging data can be directly processed onboard (*i.e.*, independently from the ground operators), they are well suited to support highly risky operations (*e.g.*, pinpoint landing), as recently demonstrated by JAXA's SLIM (Smart Lander for Investigating Moon) mission that landed on the Moon in January 2024. A key objective of the mission was to use a novel optical navigation (OpNav) technology to enable a pinpoint landing of the robot to a desired target location on the Moon [3]. An accurate localization of the lander was retrieved throughout the descent phase by establishing correspondences between the craters detected in the images acquired by the camera and reference crater maps stored on the onboard computer, leading to landing accuracies better 100 m. Craters are

also key to provide a first-guess estimate of the spacecraft state in case of lost-in-space scenarios, by matching patterns of craters between the image and an onboard catalogue [4-5]. In case an accurate catalogue of surface features is not available, other surface features can be detected, and their locations estimated, to retrieve auxiliary image-based measurements to enable deep-space navigation operations. As an example, a navigation scheme based on image data only has been proposed to enable autonomous approaching operations to unknown small bodies [6].

A joint analysis of optical and radiometric data has been used to support the orbit determination operations for spacecraft orbiting small bodies, such as the Dawn mission at Vesta, where an advanced feature extraction and matching process based on *maplets* was used to obtain auxiliary image-based measurements to constrain the spacecraft trajectory in the along- and across-track directions [7]. For missions devoted to the exploration of larger-sized bodies, such as moons or planets, however, a joint processing of imaging and radio-tracking data has not been fully explored yet. Nevertheless, a refined reconstruction of the trajectory of a planetary orbiter could support an improved estimation of key geophysical parameters. Data-fusion approaches are then key to expand the scientific return of the future exploration missions.

In this work, we preliminarily investigate an orbit determination approach based on the joint processing of radiometric and imaging data. To test and validate the data-combination scheme and the image processing algorithms, thorough numerical simulations were carried out based on a probe in a low-altitude orbit around the Moon. In the following sections, a detailed description of the algorithms used to tackle the automatic crater detection and matching is provided. After describing the orbit determination scheme and the synthetic environment used to carry out the numerical simulations, we present preliminary results of attainable trajectory reconstruction accuracies through the implemented multi-sensor orbit determination approach.

II. DATA AND METHODS

A. Precise Orbit Determination
Precise orbit determination (POD) is the process of estimating the spacecraft motion relative to the orbited

body. The spacecraft dynamics and measurements models are described by highly nonlinear equations, which are affected by errors. An iterative least-squares estimation filter is then used to adjust the model parameters to minimize the discrepancies between the data collected by the spacecraft (*i.e.*, observed data) and those predicted through the mathematical models (*i.e.*, predicted data) [8]. At each iteration, the partial derivatives of the measurements with respect to the state estimation vector are computed to retrieve the corrections δx to the model parameters, as:

$$\delta \boldsymbol{x} = (\mathrm{H^T W H} + \overline{\mathrm{P}}^{-1})^{-1}(\mathrm{H^T W}\boldsymbol{y} + \overline{\mathrm{P}}^{-1}\overline{\boldsymbol{x}}_0) \quad (1)$$

where $\overline{\boldsymbol{x}}_0$ and $\overline{\mathrm{P}}$ are the *a priori* state deviation vector and covariance matrix, respectively; H is the observation-state mapping matrix; $\boldsymbol{y}$ is the observation residual vector; and W is the (diagonal) measurement weighting matrix. The multi-sensor orbit determination approach investigated in this study is based on a combined processing of radio tracking and optical data. To retrieve a minimum variance estimation of the state parameters, each measurement included in the estimation filter is weighted based on the expected measurement noise (Sec. III). At each iteration, the model parameters are updated according to the retrieved corrections. Once convergence is declared, the covariance matrix associated with the estimated state parameters (at the reference epoch t_0) is retrieved as:

$$\mathrm{P}(t_0) = (\mathrm{H^T W H} + \overline{\mathrm{P}}^{-1})^{-1} \quad (2)$$

By using the state transition matrix $\Phi(t, t_0)$, the covariance matrix can be mapped out to time *t* as:

$$\mathrm{P}(t) = \Phi(t, t_0)\mathrm{P}_0\Phi^{\mathrm{T}}(t, t_0) \quad (3)$$

To model the optical measurements and the associated residuals, different approaches have been proposed in the literature. In this work, the following approach is used. First, craters are extracted from the collected images by using a machine learning-based approach (crater detection). For each detected crater, its diameter and center are estimated. Next, known craters from an onboard database are back projected onto the image plane according to the current estimate of the spacecraft's position and attitude (crater re-projection). Correspondences between detected and catalogue-projected craters are then established by using an approach based on the geometrical properties of crater patterns (crater identification or matching). For each pair of matched craters, row and column pixel displacements are computed between the centroid of the extracted crater and the projected centroid of the corresponding crater from the catalogue. In the following sections, an in-depth description of each step of the pipeline is provided.

B. Observed optical measurements

An accurate and autonomous detection of relevant surface features for navigation purposes is a key and challenging task. The increased maturity of machine learning techniques makes them suitable for space applications. To extract craters from the images collected by the camera, we adopted in this study a supervised transfer learning approach, where a pre-trained object detector - based on the YOLO architecture - is re-trained on a custom dataset (that includes ground truth (GT) labels and images) to learn the new crater detection task. Once the training process is completed, given an image as input, the network generates rectangular bounding boxes around candidate crater locations in the image, and assigns a confidence value to each detection. A bounding box is defined by the four-dimensional vector (x_c, y_c, w, h), where (x_c, y_c) are the column and row coordinates of the center of the box, and w and h are its width and height, respectively. For each detection, an estimate of the crater diameter (in pixel) is retrieved as an average of the dimensions of the box, as $d = (w + h)/2$.

A supervised training approach requires the definition of a GT dataset that includes images and associated labels (Fig. 1). The image dataset is retrieved by extracting 512×512 px image patches from a high-resolution (*i.e.*, 128 px/deg) global mosaic of the lunar surface that is reported in a cylindrical map projection [9]. For each extracted tile, we defined GT labels (*i.e.*, bounding boxes) according to the information reported in the crater catalogue by Wang et al. [10] that, for each crater, defines the geographic coordinates of its center (lon, lat), and the estimated crater diameter D (in metric units). Given a specific crater, the bounding box parameters are retrieved based on the mosaic map-projection as:

$$x_c = (lon \, R_M - x_{UL})/h_{RES} \quad (4)$$

$$y_c = (lat \, R_M - y_{UL})/v_{RES} \quad (5)$$

$$w = D/(h_{RES} \cos(lat)), \quad h = D/v_{RES} \quad (6)$$

where (x_{UL}, y_{UL}) are the map-coordinates of the top left corner of the mosaic; h_{RES} and v_{RES} are the horizontal and vertical mosaic pixel resolution, respectively; and R_M is the reference Moon's radius adopted in the mosaic map-projection. Note that the (lon, lat) parameters
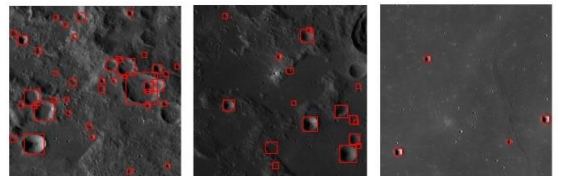

Fig. 1. *Image patches extracted from the global mosaic and associated ground truth labels (i.e., red bounding boxes).*

should be expressed in radians.

Due to map projection adopted for the mosaic, increased distortion effects are induced moving towards the poles. As a result, bounding boxes defined about craters at higher latitudes are characterized by large values of the aspect ratio that are not representative of the observation geometries accounted for in our numerical simulations, where a nadir-looking camera is considered. To enable a proper training of the network, we only extracted tiles from latitudes between $-40° \leq lat \leq 40°$. The entire dataset, which accounted for more than 1500 images, was then split into train and validation datasets by using a 75:25 split ratio. Moreover, because the mosaic is characterized by almost uniform "Sun-from-left" illumination conditions (see Fig. 1), a post-processing of the GT dataset was carried out by randomly horizontally flipping and/or rotating the images by $\pm 90°$ (the labels were modified accordingly), making the network more robust to handle different illumination conditions.

Although being trained on a dataset based on real images, the crater detector is also able to extract craters from synthetic images of the lunar surface (Fig. 2). The images are generated by using a software pipeline implemented in Blender, which allowed us to retrieve high-fidelity images that are consistent with the observation geometries accounted for in our numerical simulations. For each image acquisition, a mesh representing the observed lunar surface is created and loaded in Blender's workspace. Next, the scene is rendered by using the built-in Blender's path-tracing rendering engine according to the camera pose and the illumination conditions. Custom reflectance models have also been implemented to better represent the photometric behavior of the lunar regolith [11].

C. Predicted optical measurements

Optical residuals are computed by establishing correspondences between the craters detected in the image and those listed in the onboard catalogue. In this work, a perspective distortion-free (pinhole) camera model is considered to compute the predicted image location of the catalogue-projected craters. Given the 3D coordinates of a point in the camera frame {C} (*i.e.*, the center of the crater), $\boldsymbol{P}_C = [X, Y, Z]^T$, its 2D projection $\boldsymbol{p} = [x, y]^T$ on the image plane is retrieved as [12]:

$$\boldsymbol{p} = \mathrm{K}\widetilde{\boldsymbol{P}}_C \Leftrightarrow \begin{bmatrix} x \\ y \end{bmatrix} = \mathrm{K} \begin{bmatrix} \tilde{X} \\ \tilde{Y} \\ \tilde{Z} \end{bmatrix} \qquad (7)$$

where K is the intrinsic camera matrix, and $\widetilde{\boldsymbol{P}}_C = \boldsymbol{P}_C/Z$. The point $\boldsymbol{P}_C$ is retrieved as:

$$\boldsymbol{P}_C = \mathrm{R}_{BF}^C [\boldsymbol{r}_C - \boldsymbol{r}_{SC}] \qquad (8)$$

where R_{BF}^C is the rotation matrix from the Moon's body-fixed frame {BF} to the camera frame {C}, and $\boldsymbol{r}_C$ and $\boldsymbol{r}_{SC}$ are the crater centroid and the spacecraft position
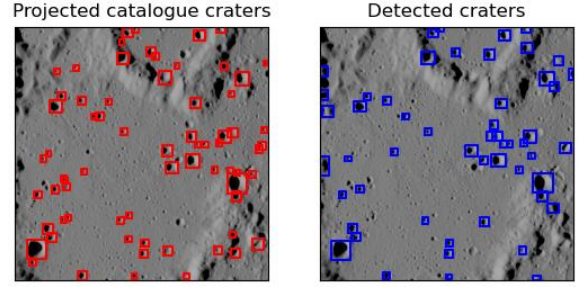

Fig. 2. *Crater detection on a synthetic image of the lunar surface. The panels show the projected craters from the Wang's catalogue (**left**), and those detected by using the YOLO-based crater detector (**right**).*

vectors referred to {BF}. The body-fixed Cartesian coordinates of the centroid of crater j are retrieved from the associated spherical coordinates $(\rho, lon, lat)_j$, as:

$$\boldsymbol{r}_{C,j} = \rho_j \begin{bmatrix} \cos(lat)\cos(lon) \\ \cos(lat)\sin(lon) \\ \sin(lat) \end{bmatrix}_j \qquad (9)$$

An accurate modeling of the radial distance of the crater with respect to the Moon's center (ρ_j) is key to correctly project its location onto the image plane. By assuming that the crater rim lies on a plane orthogonal to the vector $\boldsymbol{r}_C$, the parameter ρ represents the radial distance of the center of the crater rim with respect to the Moon's center, and can be expressed as:

$$\rho = \bar{\rho} + \Delta\rho \qquad (10)$$

where $\bar{\rho}$ is the distance of the crater floor with respect to the Moon's center, and $\Delta\rho$ is the crater's depth. An estimate of the radial distance of the crater floor with respect to the Moon's center was retrieved for each crater from a high-resolution Digital Terrain Model (DTM) of the Moon (*i.e.*, 128 px/deg, which corresponds to a resolution of $\sim$237 m/px at the equator). As regards the crater depth, an estimated value for each crater was retrieved from the Wang's crater catalogue [10].

D. Crater matching

A fundamental operation to define the optical measurements is the crater matching task, which consists in establishing correspondences between the craters detected in the image and those listed in an onboard reference database (*i.e.*, crater catalogue). In practice, the crater correspondence problem is characterized by unique challenges, because the two crater sets may be largely disjoint. As an example, the crater detector could detect unknown craters (*i.e.*, not listed in the catalogue) in the image. Similarly, it may happen that catalogued craters are not detected due to harsh illumination conditions. A robust crater matching

technique is then required to tackle this challenging task. Different approaches have been proposed to retrieve crater correspondences, including machine learning-based techniques [11], and methods based on mathematical invariants of geometric patterns of observed craters [4-5, 14] (*e.g.*, crater triads). In this work, we employed a preliminary version of a matching scheme based on crater triads (*i.e.*, each crater centroid coincides with a vertex of the triangle), which assumes that the craters are coplanar, and the camera is nadir-pointed. As a first step, two distinct sets of crater triads are defined based on the craters detected by the network (*i.e.*, observed craters) and the catalogue-projected craters (*i.e.*, predicted craters). A descriptor d_{ijk} is then computed for each crater triangle that includes the cosine of the smallest internal angle of the triangle, the cosine of the largest internal angle of the triangle, the normalized diameters of the three craters (*i.e.*, divided by the longest triangle side), and the triad orientation (based on how the internal angles are displaced) [4]. For each triad based on the detected craters, a candidate correspondent triad is found among those based on the catalogue-projected craters according to the similarity of their descriptors (Fig. 3). In this study, we are assuming that a preliminary estimate of the spacecraft state is available (*i.e.*, the spacecraft is not in a lost-in-orbit scenario), which allow us to carry out a downselection of the onboard crater catalogue based on the pose of the spacecraft camera. Craters that are expected to be outside the camera field of view (FOV) are filtered out. Because an initial orbit solution exists, a threshold on the maximum distance between the centroids of corresponding craters (*i.e.*, 10 pixel) is also applied to discard mismatched crater triads.

The output of the crater matching step is a list containing candidate pairs of corresponding craters between those detected by the network and those reported in the downsampled catalogue. Crater pairs that are ambiguous (*i.e.*, an observed crater is matched with different database craters or vice-versa) or duplicate (*i.e.*, a crater

can belong to multiple successfully matched triads) are removed from the list. Next, the row and column pixel discrepancies between the centroids of matched observed and catalogue-projected craters are computed, leading to the calculation of the optical residuals.

III. NUMERICAL SIMULATIONS

A thorough set of numerical simulations was conducted to assess the attainable orbit determination accuracies with the proposed data-fusion approach by assuming a spacecraft in a low-altitude lunar orbit similarly to the NASA mission Lunar Reconnaissance Orbiter (LRO). A covariance analysis approach was considered, with synthetic optical and radio data generated based on the integrated spacecraft trajectory and by accounting for the expected noise level of the onboard instruments. As regards the conservative forces, the spacecraft dynamical model accounts for the gravity of the Moon (through the GRGM900C model [15] in spherical harmonics to degree and order 100), and the Sun and the Earth (that are modelled as point masses). A cannon-ball model was adopted for the spacecraft to compute the non-conservative accelerations due to the solar radiation pressure. For the radiometric range-rate data, a single ground station was accounted for, and S-band Doppler accuracies were considered with a conservative root-mean-square (RMS) error of 1 mm/s at 10−s integration time [16]. A wide-angle nadir-looking camera was considered to generate the synthetic images (Table I), with an acquisition rate of 10 min and a detector size of 512×512 px, which is consistent with the size of the tiles used for the neural network training. At each new image acquisition, a synthetic image is generated by using the Blender-based pipeline that is consistent with the observation geometry (*i.e.*, acquisition epoch, spacecraft's position and orientation with respect to the Moon body-fixed frame).

The covariance analysis approach assumes that the same modeling is adopted for the dynamical forces and the onboard instruments properties between the simulation of the synthetic data and the orbit determination process, where the data are processed through a least-squares filter. The impact of each measurement type on the trajectory reconstruction is determined through the formal uncertainties of the spacecraft state. To account for unpredicted mismodeling of the dynamical
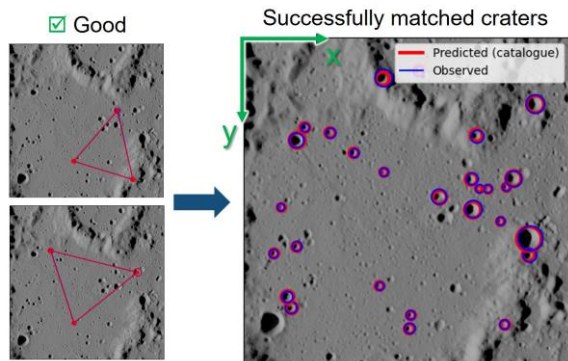

Fig. 3. *Examples of matched triads (**left**) and successfully matched craters (**right**) in a synthetic image of the lunar surface. Observed and catalogue-projected craters are shown in blue and red, respectively.*

Table 1. Characteristics of the spacecraft camera

Intrinsic camera properties	
Field of view (FOV)	90×90°
iFOV	3.91 mrad
Detector size	512×512 px
Ground resolution	195 m (@ 50 km height)
Framing mode (global shutter)	

equations, the adjusted parameters in the estimation filter include the spacecraft state at the initial epoch of the orbit determination arc and a set of periodic accelerations in the radial, transverse and normal directions. The solve-for parameters are estimated through a weighted least-squares (WLS) batch filter that minimizes the measurement residuals, where data are weighted using the expected noise for each measurement type. For the optical data, a root-mean-square error of 2 px was assumed in both the row and column image dimensions. This represents a conservative value, which was retrieved by analyzing the statistical distribution of the 2D pixel discrepancies between matched craters for a set of test images rendered at different illumination geometries.

As a future activity, we are planning to carry out a further training of the crater detector on a custom dataset that also includes synthetic images. By including images characterized by custom illumination conditions (*i.e.*, that cannot be reproduced through augmentation techniques applied on the GT dataset based on the global lunar mosaic), a more robust network would be retrieved, which is able to better cope with the great variety of observation geometries that characterize spaceborne imagery.

IV. RESULTS

The performances of the proposed data-fusion approach were evaluated by accounting for a variety of orbital configurations, including different orbit geometries (*e.g.*, face-on, edge-on, etc.) and Moon's phases. We present here the results obtained for an edge-on orbit geometry (*i.e.*, the Earth-Moon line-of-sight direction is orthogonal to the normal to the orbit plane) during a new Moon lunar phase (*i.e.*, the illuminating side is facing away from the Earth) (Fig. 4). This is a key test case to show the synergies between the radio and optical data. When the spacecraft flies over the shadowed Moon's near side, it can establish telecommunications with the
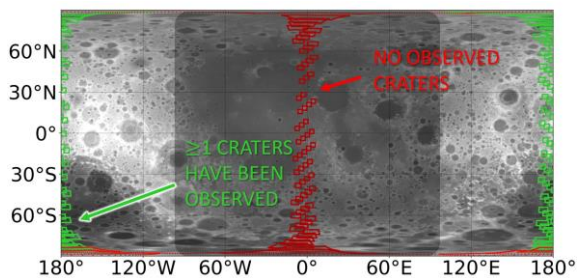
Fig. 4. *Optical data coverage during a simulated orbit determination arc (i.e., edge-on geometry and new Moon phase). The darker area indicates that the Moon's near side is in shadow. The projected camera field-of-view is shown, with green footprints indicating at least one matched crater, and red footprints indicating no observed craters.*

ground station leading to the acquisition of radio tracking data. However, no optical data are collected by the camera that operates in the visible-wavelength. On the contrary, when the spacecraft flies over the Moon's far side, no radiometric data are available because of occultations, but the collected images can provide auxiliary crater-based measurements to support the reconstruction of the spacecraft trajectory.

In Fig. 5, the 1−σ formal uncertainties of the reconstructed spacecraft trajectory are shown along the radial (top), transverse (center) and normal (bottom) directions retrieved by analyzing different datasets. By processing the optical dataset only (blue, left), higher uncertainties are retrieved compared to the solution based on radiometric data only (red, right). The shadowed magenta areas show the time periods where radio tracking data are available. The short gaps (*i.e.*, ~50 minutes) with no acquired range-rate measurements are due to occultations resulting from the edge-on spacecraft orbit geometry. The images acquired during these orbital phases thus provide auxiliary information to better constrain the spacecraft orbit. A combined analysis of radio tracking and optical data through the orbit determination filter results in enhanced uncertainties for all directions, with major improvements along the normal component (Table 2). In an edge-on geometry, the normal position component is indeed orthogonal to the line-of-sight direction, and is thus less constrained by the radiometric range-rate data. Improved orbit determination accuracies could be achieved by improving the accuracies of the optical data (*i.e.*, by reducing the optical measurement noise) and by increasing the image acquisition rate (and, thus, the number of optical data processed in the filter).

V. CONCLUSIONS

Cutting-edge data-fusion techniques are current under development to support the navigation capabilities of the future space exploration probes. A multi-sensor orbit determination approach was described in this work to retrieve a refined reconstruction of the spacecraft trajectory that is based on the joint processing of deep-space radio tracking measurements and image-based

Table 2. RMS of the 1−σ formal uncertainties of the reconstructed spacecraft trajectory in the radial, transverse, and normal directions (values in meters)

	Radial	Transverse	Normal
Optical only	61.6	64.6	54.3
Radio only	12.0	12.8	33.3
Radio + optical	8.7	9.2	19.2

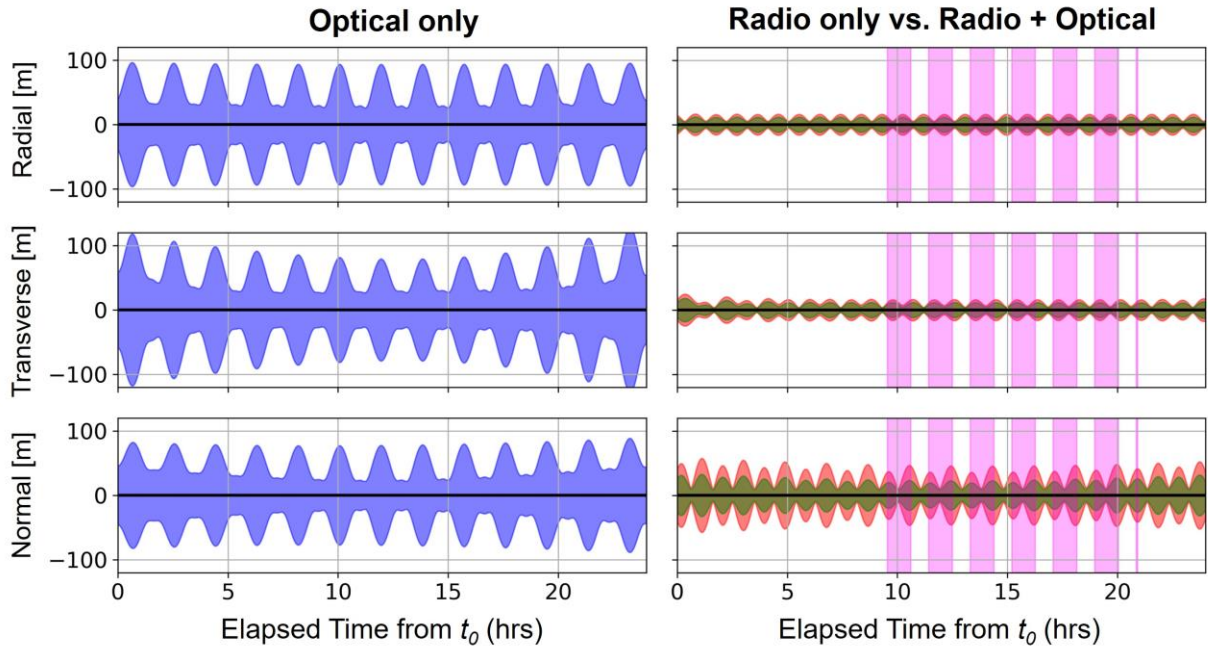**Fig. 5.** *Estimated 1−σ spacecraft position uncertainties in the Radial-Transverse-Normal (RTN) directions retrieved by processing optical data only (**left, blue**), radio tracking data only (**red, right**) and by combining optical and radiometric data (**green, right**). The magenta shadowed areas highlight the time span when radio tracking data are acquired by the ground station.*

data. The optical data are based on the matching of the observed craters in the image with those listed in an onboard catalogue. A neural network devoted to the crater detection task was then trained by using a transfer learning approach, and an automatic registration scheme was implemented to support the crater matching step.

To investigate the benefits of the proposed data-fusion approach in a realistic mission scenario, a software pipeline was implemented in Blender to generate high-fidelity synthetic images of the Moon's surface. Numerical simulations were carried out by accounting for a lunar mission scenario. Simulated radio tracking data were combined in the least-squares orbit determination filter with optical measurements extracted from synthetic images of the lunar surface. A more accurate estimation of spacecraft trajectory is enabled by the combined processing of radiometric and optical measurements compared to the solution based on radio tracking data only. Improved accuracies are observed along all the components of the spacecraft position, with major improvements along the normal direction that, in case of an edge-on orbit geometry, is orthogonal to the line-of-sight direction. This suggests that a joint processing of the two datasets is well suited to support the orbit determination process for missions devoted to the exploration of celestial bodies for which a reference catalogue of surface features is available. Nevertheless, alternative strategies have been proposed to obtain image-based measurements even if a database of known surface features is not available, including techniques that, by processing multiple observations of the same

surface area, enable a joint estimation of the spacecraft position and the body-fixed locations of the surface landmarks that are observed (*i.e.*, a catalogue of surface features is created and updated during the mission). These methodologies will be investigated as a further development of this work. In addition to explore different neural network architectures (e.g., semantic/instance segmentation networks) to tackle the crater detection and matching tasks in case of complex off-nadir geometries, we will also investigate the use of the proposed orbit determination scheme for a refined estimation of key geophysical parameters of the orbited body (*e.g.*, spin rate, pole orientation).

REFERENCES

[1] S. Asmar, "Communicating by Doppler: Detecting spacecraft dynamics during critical operations," in *SpaceOps 2012*, p. 1296119, 2012.

[2] T.A. Ely, J. Seubert, N. Bradley, T. Drain, and S. Bhaskaran, "Radiometric Autonomous Navigation Fused with Optical for Deep Space Exploration," *J. Astronaut. Sci.*, vol. 69, pp. 300-325, 2021.

[3] F. Seisuke and I. Takayuki, "Japanese lunar lander SLIM and its optical navigation for pinpoint

landing," in *Proceedings of the International Display Workshops*, 2022, p. 737.

[4] C. Hanak, T. Crain, and R. Bishop, "Crater identification algorithm for the lost in low lunar orbit scenario," in *AAS Guidance & Control Conference*, 2008.

[5] B. Maass, S. Woicke, W.M. Oliveira, B. Razgus, and H. Kruger, "Crater navigation system for autonomous precision landing on the Moon," *Journal of Guidance, Control, and Dynamics*, vol. 43, no. 8, p. 1414–1431, 2020.

[6] I.A.D. Nesnas, B.J. Hockman, S. Bandopadhyay, B.J. Morrell, D.P. Lubey, J. Villa, D.S. Bayard, A. Osmundson, B. Jarvis, M. Bersani, and S. Bhaskaran, "Autonomous Exploration of Small Bodies Toward Greater Autonomy for Deep Space Missions," *Frontiers in Robotics and AI*, vol. 8, 2021.

[7] A. Konopliv, S. Asmar, R. Park, B. Bills, F. Centinello, A. Chamberlin, A. Ermakov, R. Gaskell, N. Rambaux, C. Raymond, C. Russell, D. Smith, P. Tricarico, and M. Zuber, "The Vesta gravity field, spin pole and rotation period, landmark positions, and ephemeris from the Dawn tracking and optical data," *Icarus*, vol. 240, pp. 103–117, 2014.

[8] B.D. Tapley, B.E. Shutz, and G.H. Born, "Statistical Orbit Determination,", Elsevier, New York, 2004, Chap. 4.

[9] R. Wagner, E. Speyerer, M. Robinson, L. Team, *et al.*, "New mosaicked data products from the LROC team," in *46th Annual Lunar and Planetary Science Conference*, no. 1832, p. 1473, 2015.

[10] Y. Wang, B. Wu, H. Xue, X. Li, and J. Ma, "An improved global catalog of lunar impact craters (≥1 km) with 3D morphometric information and updates on global crater analysis," *Journal of Geophysical Research: Planets*, vol. 126, no. 9, p. e2020JE006728, 2021.

[11] J. Villa, J. Mcmahon, and I. Nesnas, "Image rendering and terrain generation of planetary surfaces using source-available tools," in *Proceedings of the 46th Annual AAS Guidance, Navigation & Control Conference*, Breckenridge, CO, USA, pp. 1–24., 2023.

[12] W. Owen, "Methods of Optical Navigation," *Advances in the Astronautical Sciences*, vol. 140, Univelt, 2011.

[13] H. Wang, J. Jiang, and G, Zhang, "CraterIDNet: An End-to-End Fully Convolutional Neural Network for Crater Detection and Identification in Remotely Sensed Planetary Images," *Remote Sens.*, vol. 10, no. 7, p. 1067, 2018.

[14] W. Park, Y. Jung, H. Bang, and J. Ahn, "Robust Crater Triangle Matching Algorithm for Planetary Landing Navigation," *Journal of Guidance, Control, and Dynamics*, vol. 42, no. 2, pp. 402-410, 2019.

[15] F.G. Lemoine, S. Goossens, T.J. Sabaka, J.B. Nicholas, E. Mazarico, D.D. Rowlands, B.D. Loomis, D.S. Chinn, G.A. Neumann, D.E. Smith, and M.T. Zuber, "GRGM900C: A degree 900 lunar gravity model from GRAIL primary and extended mission data," *Geophysical Research Letters*, vol. 41, no. 10, pp. 3382–3389, 2014.

[16] E. Mazarico, G.A. Neumann, M.K. Barker, S. Goossens, D.E. Smith, and M.T. Zuber, "Orbit determination of the Lunar Reconnaissance Orbiter: Status after seven years," *Planetary and Space Science*, vol. 162, pp. 2–19, 2018.